



# Extended electronic structure inhomogeneity created by double chain layer defects surrounding columnar tracks in heavy-ion irradiated $\text{YBa}_2\text{Cu}_3\text{O}_{7-\delta}$

Ji-Hwan Kwon<sup>1,2,7</sup> , Yifei Meng<sup>1,2</sup>, Lijun Wu<sup>3</sup>, Yimei Zhu<sup>3</sup>, Yifei Zhang<sup>4</sup>, Venkat Selvamanickam<sup>5</sup>, Ulrich Welp<sup>6</sup>, Wai-Kwong Kwok<sup>6</sup> and Jian-Min Zuo<sup>1,2,8</sup> 

<sup>1</sup> Department of Materials Science, University of Illinois at Urbana-Champaign Urbana, IL 61801, United States of America

<sup>2</sup> Frederick Seitz Materials Research Laboratory, University of Illinois at Urbana-Champaign, Urbana, IL 61801, United States of America

<sup>3</sup> Department of Condensed Matter Physics and Materials Science, Brookhaven National Laboratory, Upton, NY 11973, United States of America

<sup>4</sup> SuperPower Corp., Schenectady, NY 12304, United States of America

<sup>5</sup> Department of Mechanical Engineering and Texas Center for Superconductivity, University of Houston, 4800 Calhoun Rd., Houston, TX 77204-4006, United States of America

<sup>6</sup> Materials Science Division, Argonne National Laboratory, Argonne, IL 60439, United States of America

<sup>7</sup> Division of Industrial Metrology, Korea Research Institute of Standards and Science, Daejeon 34113, Republic of Korea

E-mail: [jjanzuo@illinois.edu](mailto:jjanzuo@illinois.edu)

Received 4 June 2018, revised 30 July 2018

Accepted for publication 6 August 2018

Published 31 August 2018



## Abstract

In  $\text{YBa}_2\text{Cu}_3\text{O}_{7-\delta}$  (YBCO), heavy-ion irradiation creates continuous amorphous tracks that are highly effective for vortex pinning. However, the electronic structure landscape of defects and consequently their vortex pinning roles are unclear. Here, we show double chain layer (DCL) defects which intersect the columnar tracks are additionally produced by high energy Pb ion irradiation in YBCO. The DCL defects are  $\sim 29$  nm long, about three times the columnar defect diameter. The electronic structures of the DCL and columnar track defects were determined using atomic-resolution scanning transmission electron microscopy (STEM) and high resolution electron energy loss spectroscopy (EELS). Results show a decrease in the oxygen and copper content at the interface between the track and the YBCO matrix, resulting in interfacial strain. For the DCL defects, the STEM/EELS study revealed a localized electron doped  $\text{CuO}_2$  plane next to the DCL defect. The DCL defects thus further extend the electronic inhomogeneity into YBCO.

**Keywords:** scanning transmission electron microscopy, electron energy loss spectroscopy, high temperature superconductor, double chain layer defect, critical current

(Some figures may appear in colour only in the online journal)

## 1. Introduction

The maximum electrical current ( $J_c$ ) that can be carried in superconductors is determined by its vortex pinning defects.

<sup>8</sup> Author to whom any correspondence should be addressed.

In the technologically important high temperature superconducting (HTS) wires based on epitaxial YBCO films, nanometer-sized and insulating defects such as BaZrO<sub>3</sub> (BZO) are intentionally introduced in a small volume fraction for vortex pinning [1]. Further enhancement in vortex pinning is achieved by organizing these defects into nanorods using the process of spontaneous phase separation and/or strain-driven ordering [2–7]. An alternative approach to introducing rod-like defects is to use irradiation with high energy heavy-ions [8]. Continuous amorphous tracks are formed in the target YBCO material under certain ranges of parameters—such as weight and energy of the ions, thermal and electric conductivity of the target, and the rate of energy transfer. In single crystal YBCO, typical track diameters fall in the range of 5–10 nm [8–11]. These tracks are known to be the most effective vortex pinning centers in YBCO, and their pinning effects have been extensively studied in single crystals [12, 13]. These tracks can also be introduced at arbitrary angles and over a wide range of areal density [14–16], allowing for design of the pinning landscape and the superconducting critical current [17].

Previous studies showed that the irradiation tracks are columnar defects of amorphized material [10, 11]. The same study also suggested that a region of stacking faults, surrounding the irradiation tracks and the related strain field, propagate into the crystal lattice [10]. Further, the electron energy loss spectroscopy (EELS) study demonstrated a significant modification in the oxygen *K* edge pre-peak in the electron energy loss near edge structure, which suggests a decrease in the number of holes in the crystal near the amorphous region [10]. In addition, the strain fields surrounding the columnar defects induce local oxygen reordering [18]. All these results indicate that the effects of the columnar defects extend further into the crystalline matrix.

Here, we show that high energy Pb ion irradiation at splay angles of  $\pm 45^\circ$  produces additional double chain layer (DCL) defects in YBCO, which intersect the columnar tracks. These DCL defects further extend the electronic structure modification into the YBCO matrix. We investigated the electronic structure of defects using the latest electron aberration correction technology in STEM/EELS with significantly improved spatial resolution. STEM/EELS measurements revealed that the O *K* edge in the plane immediately adjacent to the DCL has a smaller pre-peak compared to the reference O *K* edge that is away from the DCL. The Cu *L* edge in the plane next to the DCL also shows an additional small peak at  $\sim 934$  eV corresponding to Cu<sup>1+</sup>, indicating electron doping, and this doping is localized within a single crystal unit cell. The same EELS measurements across the irradiation tracks also revealed that the amount of oxygen and copper decreases at the interface of the irradiation track and the YBCO matrix, resulting in interfacial strain.

## 2. Experiment

The commercial YBCO coated conductor (without BZO nanorods) used in this study was grown by SuperPower, Inc. [19]. The YBCO coated conductors with thickness of  $\sim 1$   $\mu\text{m}$  were grown on Hastelloy substrates using metal–organic

chemical vapor deposition. The in-plane texture in the MgO buffer layer located between the superconductor and the substrate was achieved using an ion beam assisted deposition process [20]. The engineering current density,  $J_e$ , of the YBCO film was  $\sim 410$  A cm<sup>-1</sup> width at 77 K and 0 T, corresponding to a critical current density  $J_c \sim 4.1$  MA cm<sup>-2</sup>. The samples were irradiated at the ATLAS facility at Argonne National Laboratory with 1.4 GeV <sup>208</sup>Pb ions to a cumulative dose-matching field of 2 T ( $9.67 \times 10^{10}$  ions cm<sup>-2</sup>) [12], with 1 T at splay angles of  $\pm 45^\circ$  from the normal of the film each. The dose-matching field corresponds to the irradiation dose where each vortex will be pinned by a defect at a particular magnetic field. By using a low enough Pb ion beam current, heating effects were minimized and the transition temperatures of all the YBCO samples remained nearly the same after irradiation [17].

Cross-sectional TEM samples were prepared by focused ion beam (Helios 600, FEI) patterning. Scanning transmission electron microscopy was performed using the JEOL-ARM200F (S)TEM installed at Brookhaven National Laboratory and the JEOL 2200F (S)TEM at the University of Illinois (the performance of JEOL 2200F was report in [21]). The JEOL-ARM200F was equipped with a cold-FEG and a GIF Quantum ER EELS spectrometer. The energy resolution was measured at 0.6 eV. We used both the annular bright field (ABF) detector and the high angle annular dark field (HAADF) detector in the JEOL-ARM200F. The cut off angle for ABF imaging was 11–22.4 mrad and 67–275 mrad for HAADF imaging. All observations were carried out using electrons of 200 keV in energy. For STEM-EELS performed using the JEOL-ARM200F, the collection angle was 90 mrad and the beam convergence angle was 21.2 mrad. For EELS data analysis, the background subtraction was performed using the power-law model as implemented in Gatan Digital Micrograph software.

Aberration corrected STEM/EELS was used since it significantly extends our capability for characterizing the electronic structure of YBCO. For example, Gauquelin *et al* presented an atomically resolved electronic structure study of both doped and undoped bulk YBCO. Their results showed a fine structure difference between chains and planes at both Cu *L* and O *K* edges [22]. The *L* spectra of planar Cu remained almost the same upon oxygen doping, while the O *K* edge showed a lower energy peak corresponding to the doped hole states running through  $E_F$  (Zhang–Rice singlet band [23]).

## 3. Results and discussion

### 3.1. Columnar defects in Pb-irradiated YBCO

Figures 1(a) and (b) show examples of STEM images recorded from the Pb ion irradiated YBCO sample, using the STEM HAADF and ABF detectors respectively. The marked in-plane direction (normal to the *c*-axis) of YBCO is approximately horizontal in the images. Various defects are observed in the irradiated YBCO, namely the irradiation tracks and precipitates. The irradiation tracks, running along the diagonal direction are observed in dark contrast in the HAADF-STEM image. The irradiation tracks appear to be



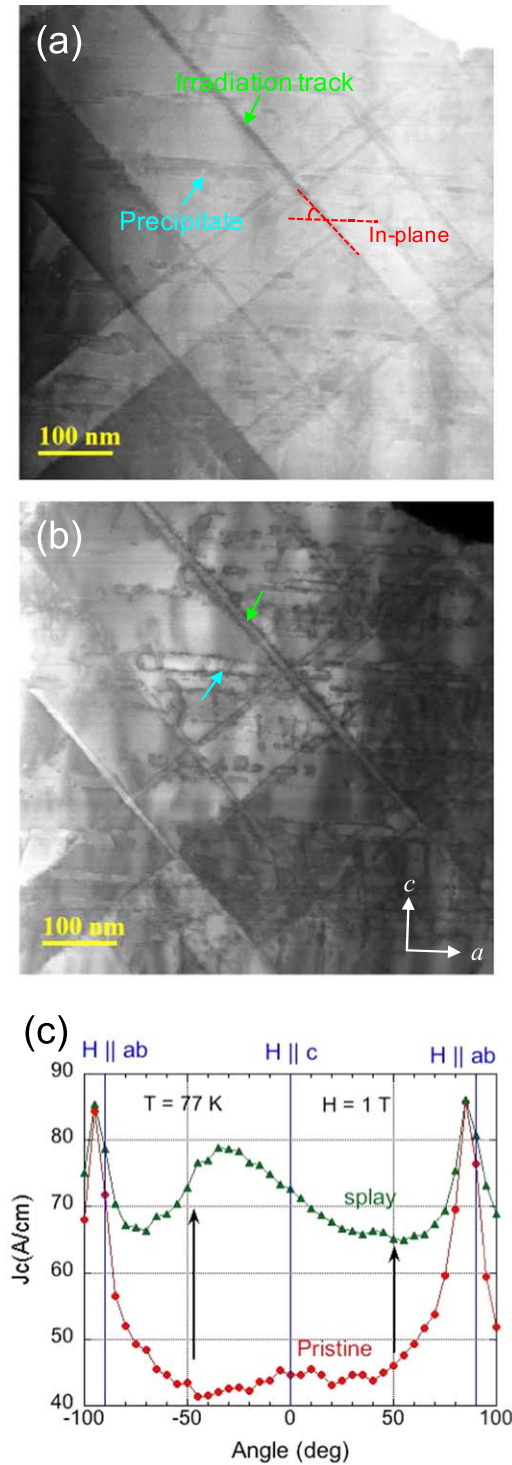


**Figure 1.** Medium-magnification STEM images of Pb ion irradiated YBCO. (a) HAADF image and (b) ABF image. (c) Angular dependence of  $J_c$  of the pristine and  $\pm 45^\circ$  irradiated samples at 77 K and 1 T.  $J_c(\theta)$ -performance is significantly improved by the incorporation of splayed columnar defects.

straight and continuous and their directions are consistent with the irradiation directions, i.e.  $\pm 45^\circ$  with respect to the marked in-plane direction. The same irradiation tracks appear in bright contrast with dark contrast at the edges in the ABF-STEM image. Elongated precipitates are observed along

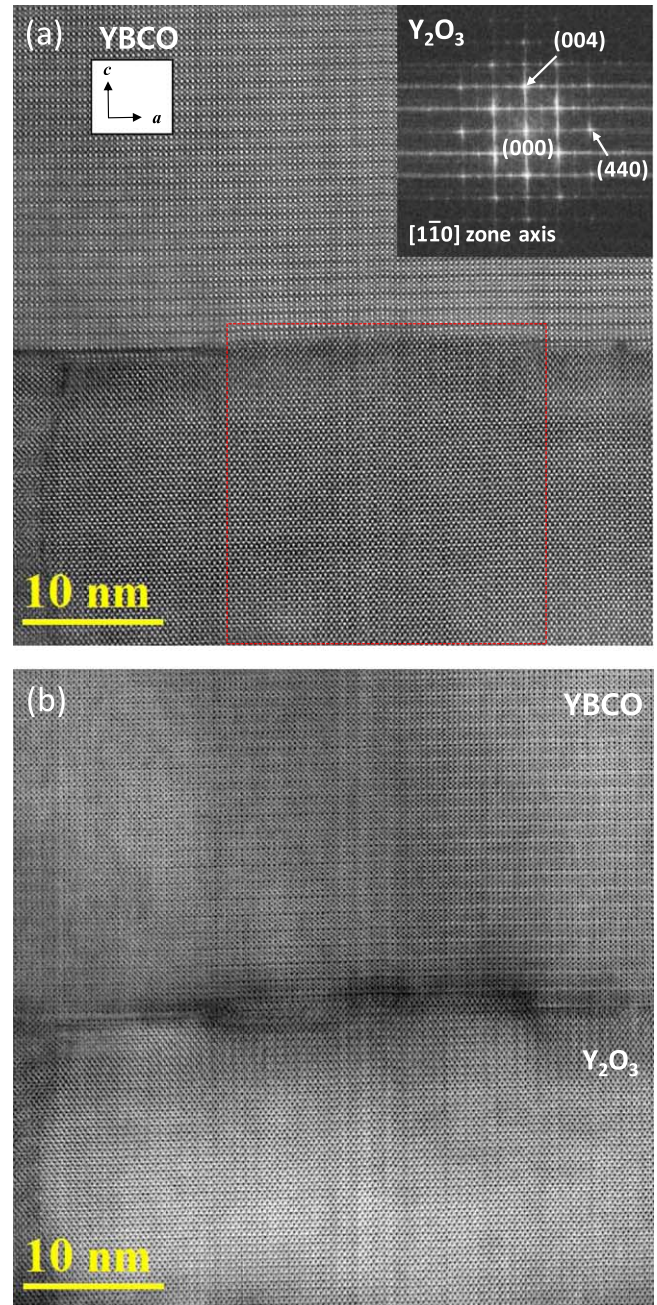


**Figure 2.** (a) Atomic-resolution ADF-STEM image, (b) ABF-STEM image of  $Y_2O_3$  precipitate embedded in YBCO. Inset shows the fast Fourier transform from the boxed region of the precipitate. The orientation relationships between  $Y_2O_3$  and YBCO are derived as  $(001)Y_2O_3 \parallel (001)YBCO$  and  $(110)Y_2O_3 \parallel (100)YBCO$ .

the in-plane direction; their lengths vary from several tens of nanometers to hundreds of nanometers and their thicknesses are around 10 nm. We noticed that the defects are more clearly seen in the ABF image that contains diffraction contrast.

The angular dependence of  $J_c$  of the irradiated YBCO tape is compared with the pristine YBCO tape in figure 1(c). The  $J_c$  value of the irradiated YBCO tape is significantly enhanced over the entire angular range except the point at  $H \parallel ab$  where the maximum  $J_c$  value is retained. The splayed columnar defects produced by the heavy ion as shown in figures 1(a) and (b) play



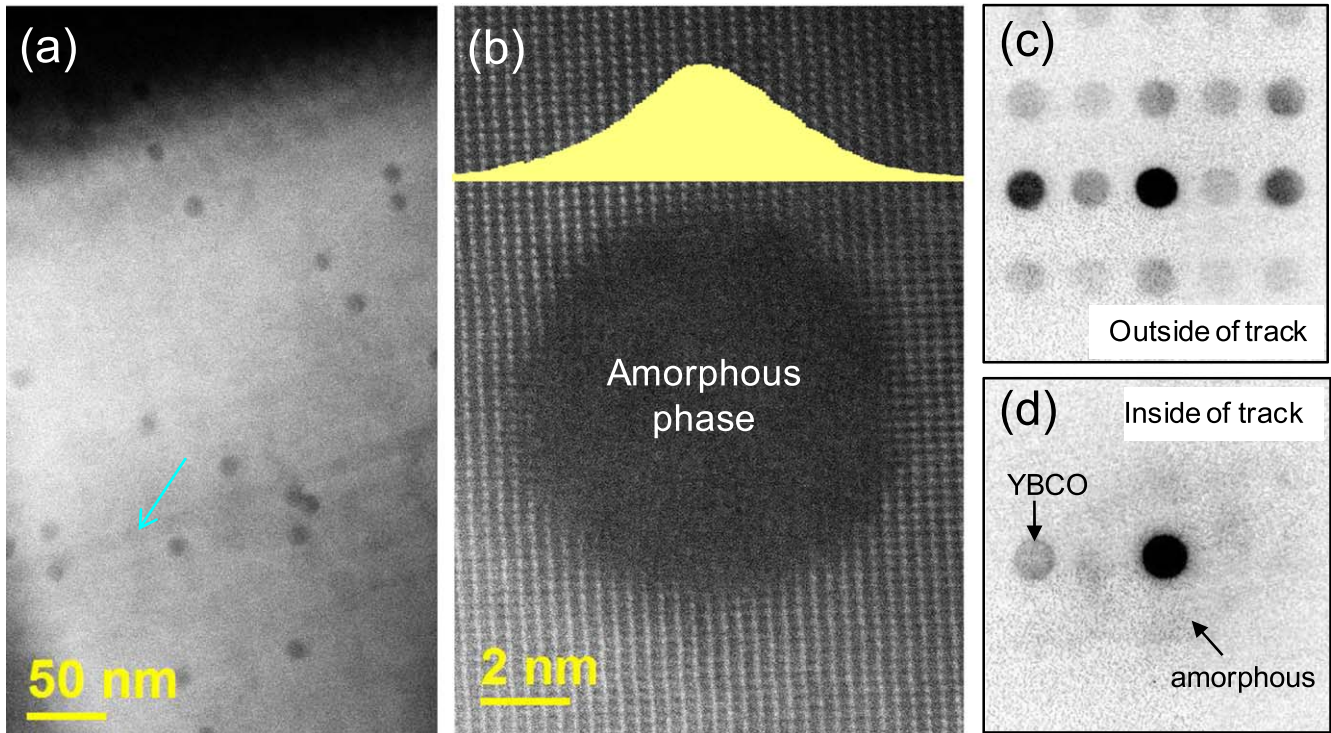


**Figure 3.** A top view of Pb-irradiation tracks. (a) Medium-magnification HAADF image of irradiation tracks. The band-like contrast as marked by the arrow is attributed to one of the irradiation tracks along the other direction ( $-45^\circ$ ), (b) atomic-resolution HAADF image of an irradiation track, (c) electron diffraction pattern of YBCO, and (d) electron diffraction pattern of the irradiation track in (b). The electron beam intensity profile used for electron diffraction is overlaid in (b).

effective vortex pin centers, and enhance the lowest  $J_c$  values in the range between  $-50^\circ$  and  $50^\circ$ , which consequently improves the overall anisotropy of the  $J_c$  value: the anisotropy of  $J_c$  defined as  $J_c(\text{max})/J_c(\text{min})$  decreased from 2.02 in pristine YBCO to 1.31 in irradiated YBCO.

To identify the pre-existing precipitates, we performed high resolution STEM. Figures 2(a) and (b) show two atomic resolution images of a precipitate in the YBCO film. The images confirm that the precipitates are  $\text{Y}_2\text{O}_3$  and the fast Fourier transform is shown in the inset. The  $\text{Y}_2\text{O}_3$  precipitates are also observed in the un-irradiated YBCO coated conductor as they are pre-existing defects in the YBCO film. The orientation relationships between  $\text{Y}_2\text{O}_3$  and YBCO are  $(001)\text{Y}_2\text{O}_3 \parallel (001)\text{YBCO}$  and  $(110)\text{Y}_2\text{O}_3 \parallel (100)\text{YBCO}$ , which are consistent with previous reports [24]. Closer observation using ABF-STEM (figure 2(b)) reveals some fuzzy dark contrast near the interface between the precipitate and the YBCO matrix. A similar dark contrast is also observed near the irradiation track as shown in figure 1(b).

The size and distribution of the irradiation tracks were measured from a cross-sectional specimen, which was prepared perpendicular to the irradiation direction ( $+45^\circ$ ) for a top view of some irradiation tracks. A medium-magnification image is displayed in figure 3(a) showing the irradiation tracks in the  $+45^\circ$  direction in dark, dot-like, contrast. The image reveals a random distribution of these irradiation tracks. The band-like contrast as marked by the arrow in figure 3(a) can be attributed to one of the irradiation tracks along the other direction ( $-45^\circ$ ). Interestingly, this particular track appears to intersect two of the tracks along

the  $+45^\circ$  direction within the image's field of view. Using images like figure 3(a), we measured the sizes of the irradiation tracks to be  $10.8 \pm 1.1$  nm in diameter on average. The density of the irradiation track based on the top view image is calculated as  $\sim 1.7 \times 10^{10} \text{ cm}^{-2}$ . Since the irradiation tracks are scattered with a Poisson distribution, locally, their distribution can easily vary by a factor of two or three.

Figure 3(b) shows a top view of an irradiation track at atomic resolution as recorded along  $[101]$  of YBCO. The HAADF-STEM image shows clearly the arrangements of atomic columns of YBCO, except inside the irradiation tracks, indicating that these tracks are amorphous. The electron diffraction patterns shown in figures 3(c) and (d) were taken from the YBCO film and the irradiation track, respectively. Figure 3(d) shows a ring pattern that can be attributed to the amorphous phase inside the irradiation track. The electron diffraction patterns were recorded using the technique of scanning electron nanodiffraction in a JEOL-2100 TEM operated at 200 kV [25]. The electron beam was focused to  $\sim 4$  nm in diameter (its intensity profile is plotted and overlaid in figure 3(b)). Note that one diffraction spot in figure 3(d) came from the tail of the electron beam overlapping the adjacent YBCO matrix.

### 3.2. DCL as secondary defects

The HAADF/ABF-STEM images of the irradiation tracks recorded at high magnifications shown in figures 4(a) and (b) revealed secondary defects associated with the irradiation

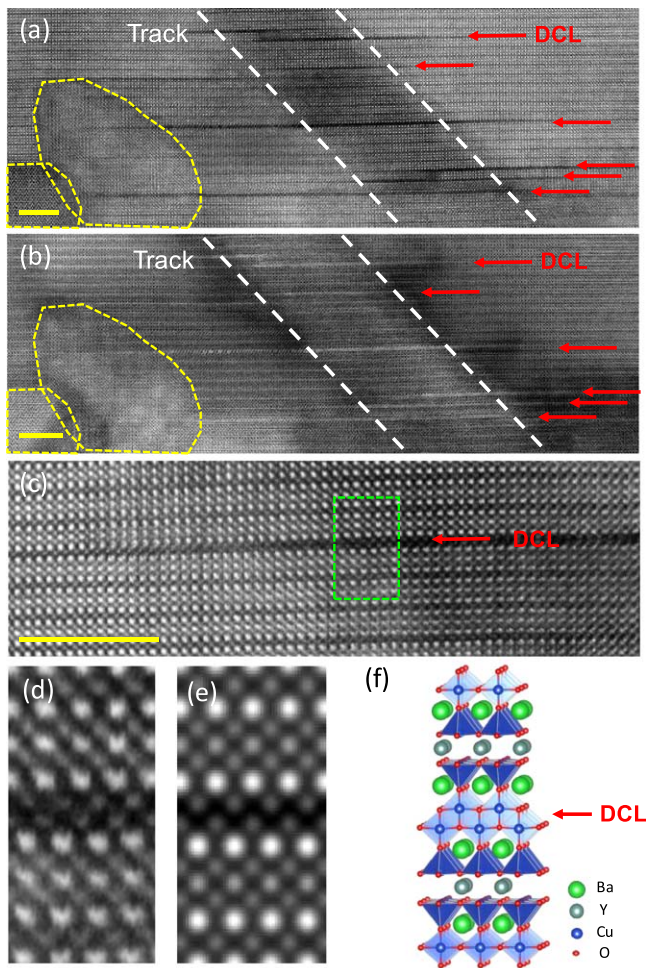


**Figure 4.** (a) HAADF and (b) ABF-STEM images of a Pb ion irradiation track in the YBCO layer. (c) Atomic-resolution HAADF-STEM image of a double chain layer in the Pb ion irradiated YBCO. (d) An enlarged atomic-resolution HAADF-STEM image, and (e) the simulated HAADF-STEM image of the double chain layer. (f) An atomic structure model of the double chain layer in YBCO. The scale bars in (a)–(c) are 5 nm. Here, DCL refers to the double chain layers. The STEM images of (a) and (b) show that the secondary defects are associated with the irradiation track. The parallel dashed lines indicate the irradiation track while the thin encircled regions are secondary defects.

tracks, which are marked by arrows and labeled as DCL. These defects run along the in-plane direction. The atomic structure of one of the planar defects is shown in figures 4(c)–(e) at atomic resolution. The electron image simulation of HAADF-STEM (figure 4(e)) identifies these defects as DCL defects caused by the insertion of extra Cu–O chains between the BaO layers in YBCO (the simulation was carried out using the ZMULT program, based on the multi-slice method described in [26]). A model of its atomic structure is displayed in figure 4(f) [27]. In ABF-STEM, the DCLs appear as bright contrast, which is consistent with the sensitivity of ABF-STEM to light atoms [28].

Interestingly, these DCL defects are found mostly near the irradiation tracks. The distribution of these planar defects is rather random and the average length of the double chain defect is measured at  $29.0 \pm 8.7$  nm. The density of the

double chain defects per length of the irradiation track is measured to be  $0.072 \text{ nm}^{-1}$ . (Secondary phases found in figures 4(a) and (b) are also marked; one is  $\text{Y}_2\text{O}_3$  as discussed previously and the other is not identified.)

The existence of double chain layer defects in YBCO has been widely reported, for example, in strained YBCO thin films [29], in YBCO that contains  $\text{BaZrO}_3$  precipitates [30] as well as in pristine YBCO crystals [27]. The DCL defects found near the irradiation track are likely produced during ion irradiation due to the strain caused by the formation of interfaces between the amorphous [10] and crystalline YBCO phase and diffusion of Cu and O ions (see further discussions below).

The extra Cu–O chains are also present in other YBCO-derived phases, such as  $\text{YBa}_2\text{Cu}_4\text{O}_8$  (Y124) [31] and  $\text{Y}_2\text{Ba}_4\text{Cu}_7\text{O}_{14+x}$  (Y247) [32]. The Y124 phase contains the DCL instead of single Cu–O chain as observed in  $\text{YBa}_2\text{Cu}_3\text{O}_{7-x}$  (Y123). The Y124 phase is reportedly more stable at higher temperatures in terms of oxygen content than the Y123 phase. On the other hand, the Y247 phase shows an intermediate structure between Y123 and Y124; it consists of Y123 type blocks that have the single, corner sharing Cu–O square-planar chains, which alternate with the Y124 type blocks containing double edge-sharing Cu–O square-planar chains. Both Y124 and Y247 phases show superconductivity with a  $T_c$  at  $\sim 81$  K and  $\sim 40$  K, respectively. The DCL defect is reported to be adverse to thin film superconductivity; the YBCO films that partly contain Y124 or Y247 phase have a lower  $T_c$  compared to the YBCO films without the double chain intergrowth [33]. In addition, Kagawa *et al* [34] reported that the Cu–O double chains are not responsible for superconductivity in Y124 single crystals based on the fact that superconductivity should be quite anisotropic with respect to the  $a$  and  $b$  axes. Indeed, torque magnetometry yields a superconducting in-plane anisotropy of  $\gamma_{ab} = 1.12 \pm 0.06$ , which is much smaller than the value of  $\gamma_{ab} = 3$  deduced from the  $ab$  anisotropy of the normal-state resistivity [34].

### 3.3. Interface between irradiation tracks and the YBCO matrix

In the ABF-STEM image shown in figure 1(b) (see also figure 4(b)), dark contrast is observed along the edges of the irradiation tracks. This dark contrast is absent in the HAADF image (see figures 1(a) and 4(a)), whose contrast is based largely on the atomic numbers, e.g.  $Z^n$  with  $n \sim 2$  [35]. The dark contrast in ABF is thus related to the strain or oxygen content or both at the irradiation track/YBCO interface. To understand the nature of the dark contrast at the interface, we carried out an EELS study by acquiring EELS line scans across the irradiation track as shown in figures 5(a), (c). Figures 5(b), (d) show the line profile of the integrated O  $K$  edge and Cu  $L$  edge intensities over an energy window of 40 eV for both spectra, which are plotted together with the HAADF signal. As indicated by the arrow in figures 5(b), (d), the amounts of O and Cu decrease at the interface. Previously, Cantoni *et al* [36] showed a similar dark contrast at the interface of nano-column BZO/YBCO in ABF images, which they attributed to strain. These authors also found oxygen



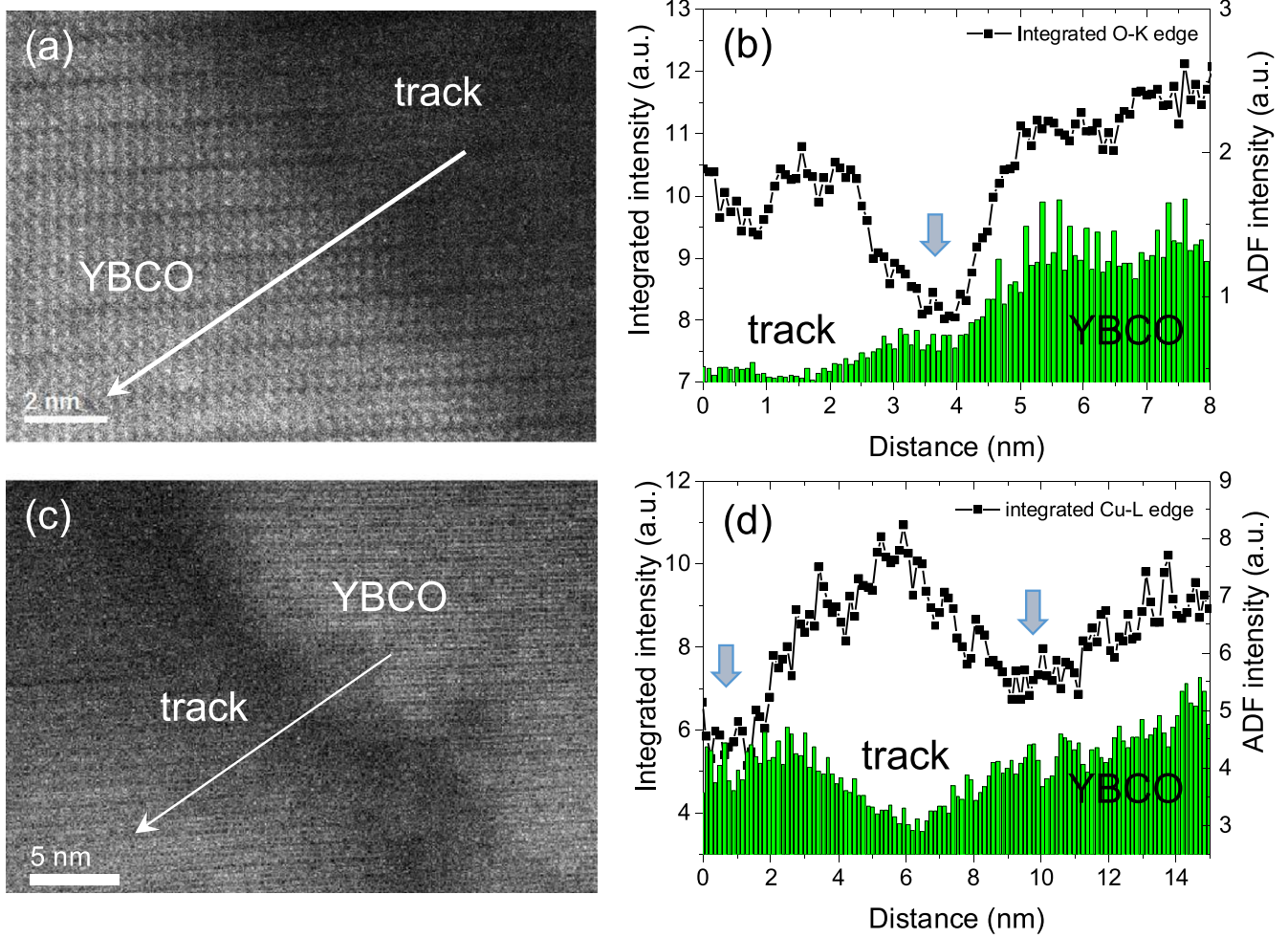


**Figure 5.** (a), (c) HAADF images showing where the EELS line scans were performed. (b) Line profile of the integrated O K edge. (d) Line profile of the integrated Cu L edge.

deficiencies at the BZO/YBCO interface, from which they inferred that the oxygen deficiency resulted from the large strain caused by a dislocation region at the BZO/YBCO interface. In our samples, the Pb ion irradiation introduces the interfaces between the amorphous and crystalline phases as well as a reduction of the O and Cu contents at the interface [10]. We speculate that some of the released interfacial O and Cu diffuses into neighboring areas, resulting in the formation of DCLs near the irradiation tracks.

The extent of O and Cu reduction is measured from the obtained EELS scans by measuring the full-width at half maximum of reduced integrated intensity. The results show that the average spreads of O and Cu reduction are 3.29 nm and 3.12 nm, respectively. However, the reduction of O and Cu is not uniform along the irradiation track; it ranges from 1.70 to 5.38 nm for O and 2.12 to 5.40 nm for Cu. Note that the size of the irradiation track depicted in the ABF image is  $\sim 3.5$  nm larger than in the ADF image (for each side) due to the dark contrast shown in the ABF image near the irradiation track, and the average extended distance measured in the ABF image is similar to the extent of O and Cu reduction measured with EELS.

### 3.4. Electronic structure of DCL defects

To elucidate the electronic structure of DCL, and especially in order to study the impact of the DCL on the electronic structure in the neighboring layer, an atomic-resolution EELS study was performed across the DCL. The closest  $\text{CuO}_2$  plane from the double chain was chosen (referred to as 1st plane) and compared with the other plane layers (2nd plane) that are separated from the double chain by more than two unit cells. Figures 6(a), (b) show O K and Cu L edges in the plane layers. At the O K edge in the plane, two peaks are observed: the pre-peak with onset of  $\sim 527.5$  eV and the main peak. The pre-peak of the O K edge of the 2nd plane layer, which corresponds to the doped hole states running through  $E_F$  (Zhang–Rice singlet band), was observed, which agrees well with the previous result [22]. At the O K edge of the 1st plane, however, the pre-peak is rather decreased in intensity, which may imply that the 1st plane layer is slightly less hole-doped as compared to the 2nd plane layer [10].

The Cu L edge shows two peaks:  $\text{Cu } L_3$  and  $\text{Cu } L_2$ , arising from transition of  $2p_{3/2} \rightarrow 3d_{3/2}3d_{5/2}$  and  $2p_{1/2} \rightarrow 3d_{3/2}$ , respectively. The measured  $\text{Cu } L_3$  peak of  $\sim 931.5$  eV at the 2nd plane layer is in good agreement with previous reports

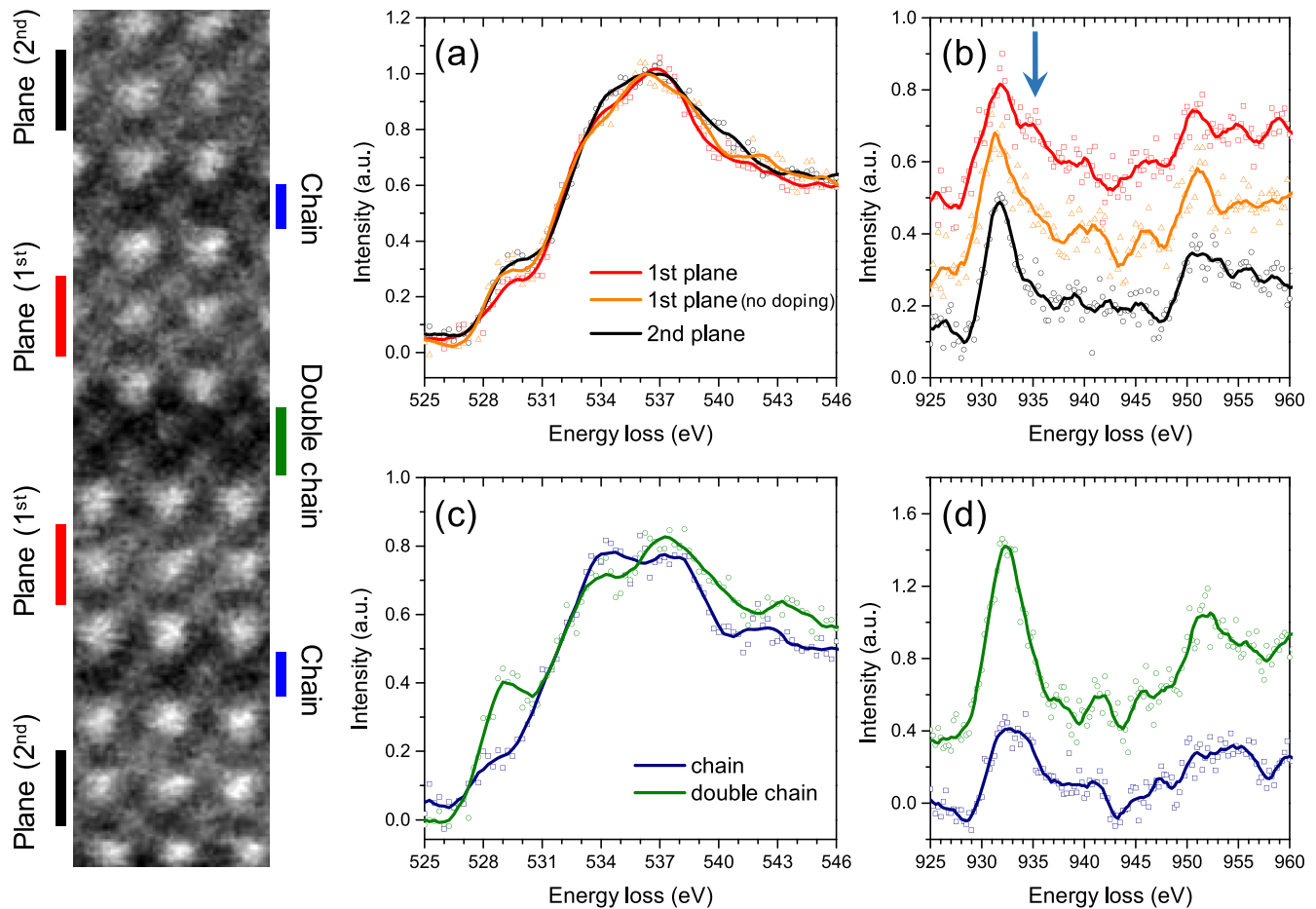


**Figure 6.** (a) O  $K$  edge and (b) Cu  $L$  edge of a plane layer taken from the first unit cell and second unit cell from the double chain layer. (c) O  $K$  edge and (d) Cu  $L$  edge of plane layer taken from the double chain and chain layer, respectively. The lines are drawn by the smoothing of raw data points using the Savitzky–Golay method. Note that Cu  $L$  edges in (b) and (d) are shifted vertically for clear visualization.

[22]. The peak at  $\sim 931.5$  eV corresponds to  $\text{Cu}^{2+}(3d^9)$  [22]. However, at the 1st plane layer, the Cu  $L_3$  edge shows an additional peak at  $\sim 934$  eV, which corresponds to  $\text{Cu}^{1+}$  in  $\text{Cu}_2\text{O}$  [37]. Previously, Gauquelin *et al* [22] showed that the Cu  $L_3$  edge in the plane layer does not change with oxygen doping: both undoped and doped YBCO showed Cu  $L_3$  edges peaked at  $\sim 931.5$  eV, claiming that doped holes in the plane layers mainly go into O- $2p$  rather than Cu- $3d$  states. However, the  $\text{CuO}_2$  plane adjacent to the DCL shows a different oxidation state, i.e.  $\text{Cu}^{1+}$ , indicating that electron doping is introduced in the  $\text{CuO}_2$  plane layer by the DCL.

We also observed that at some locations the Cu  $L_3$  edge in the 1st plane layers does not show a peak at  $\sim 934$  eV, but the spectrum is similar to the 2nd plane layers (which is plotted in orange in figure 6(b)). In addition, in the regions where such phenomenon is observed, the O  $K$  pre-peak appears similar to, or slightly smaller than, the pre-peak observed in the 2nd plane. These observations suggest that some regions are not electron doped or only have a small amount of electron doping. Thus, the electron doping effect is not uniform in the  $\text{CuO}_2$  planes adjacent to the DCL defect.

Figures 6(c) and (d) show the O  $K$  and Cu  $L$  edges from the chain and DCL, respectively. A large difference is found in the pre-peak of the O  $K$  edge: a high intensity pre-peak at

$\sim 529$  eV is observed in the DCL while a small bump is found in the chain layer at this energy level. In previous studies of the EELS spectra of the chain and plane layers of YBCO [22], the pre-peak in the O  $K$  edge from the chain layer was taken as an indication of the concentration of electron–holes in the chain layer; the O  $K$  edge in the chain had a significant pre-peak intensity in doped YBCO, whereas the undoped YBCO was absent of pre-peak intensity. Note that the pre-peak intensity of the chain layer observed here is not as pronounced as the one observed in Gauquelin *et al* [22], which could be attributed to the different EELS resolution. In addition, the Cu  $L$  edge in figure 6(d) shows noticeable changes between chain and DCL, e.g., the intensity of the DCL is higher than that of the chain layer. Also, the chain layer shows two peaks at  $\sim 931.5$  eV and  $\sim 934$  eV, corresponding to  $\text{Cu}^{2+}$  and  $\text{Cu}^{1+}$ , respectively [22]. In contrast, the DCL has only a single peak at  $\sim 931.5$  eV, which indicates that the DCL is mostly composed of  $\text{Cu}^{2+}$ .

### 3.5. Other planar defects induced by heavy-ion irradiation and vortex pinning

Planar defects of morphology similar to the DCL defect were reported before in YBCO irradiated by heavy-ions [38]. The

planar defects are believed to be generated during irradiation of the high energy ions. The observed planar defects extends from three to five times the radius of the amorphous irradiation track. In comparison, the average length of the DCL defects observed here is 5.4 times the track radius. The formation and the structure of planar defects are dependent on the condition of the samples and the nature of irradiating ion. For example, the planar defects reported for YBCO irradiated with 300 MeV  $\text{Au}^{+24}$  and 276 MeV  $\text{Ag}^{+21}$  have several structures, as observed by high resolution electron microscopy, including the DCL identified here [38]. These planar defects were generated by the ion beam oriented parallel to the  $a$ - $b$  plane. They are spaced close to each, and they are parallel to the irradiation track. In contrast, the DCL defects observed here are stacked along the amorphous track. Two models have been suggested for the formation of planar defects during ion irradiation, one is the regrowth model and the other is the strain model [38]. In the regrowth model, the defects form during the regrowth of the molten zone created by the thermal energy deposited by the irradiating high energy ions. In the strain model, the defects are formed by the release of strain created by the expansion of the amorphized volume. Both models suggest that the formation of the planar defects is a general feature in the heavy-ion irradiated YBCO.

For HTS, defects of sizes close to the coherence length  $\xi$  act as pinning centers of magnetic flux lines and enhance the properties of superconductors, such as higher critical current and better performance under high magnetic field. Unlike the extended defects, which take up significant volume and block the supercurrent flow, the small defects are considered as 'good defects'. Previous studies have identified point defects, certain types of dislocations and small angle grain boundaries, small precipitates, artificially introduced irradiation tracks and twin boundaries as 'good defects' for flux line pinning. The DCL defects are similar to the small angle grain boundaries and twin boundaries in their 2D geometry. Our EELS study demonstrates that the effects of the DCL defect extend into the neighboring Cu-O plane, giving rise to an effective thickness of  $\sim 1$  nm, which are comparable to  $\xi$  in YBCO. Since the DCL defects are stacked along the irradiation track, their strategic distribution further enables the optimization of the concentrations of defects in YBCO for maximal critical current [17].

#### 4. Conclusion

We have studied the atomic and electronic structure of Pb-irradiation defects in YBCO coated conductors. A splayed Pb-irradiation at  $\pm 45^\circ$  produces an amorphous columnar defect track with a diameter of  $10.8 \pm 1.1$  nm. The atomic-resolution HAADF-/ABF-STEM images revealed DCL defects associated with the irradiation-induced tracks. We obtained the electronic structure of the DCL and the neighboring layer in a layer-by-layer fashion from atomic-resolution EELS, showing that the  $\text{CuO}_2$  plane layer adjacent to the DCL contains more electrons than the one next to a single chain layer, delineating an atomically localized electron doped  $\text{CuO}_2$  plane layer. The EELS results also showed that

the amount of oxygen and copper is decreased at the interface between the irradiation track and the YBCO matrix over a length of  $\sim 3$  nm. These results together provide fundamental knowledge about irradiation-induced defects in YBCO coated conductors. In particular, the interspersed DCL defects reported here were not known before and their presence further extends the electron state inhomogeneity into the YBCO matrix.

#### Acknowledgments

This material is based upon work supported as part of the Center for Emergent Superconductivity, an Energy Frontier Research Center funded by the US Department of Energy, Office of Science, Office of Basic Energy Sciences, under award number DE-AC0298CH10886. LW and YZ were funded by the US Department of Energy, Office of Basic Energy Science, Division of Materials Science and Engineering, under Contract No. DE-SC0012704.

#### ORCID iDs

Ji-Hwan Kwon  <https://orcid.org/0000-0002-5024-2644>

Jian-Min Zuo  <https://orcid.org/0000-0002-5151-3370>

#### References

- [1] Ercolano G, Harrington S A, Wang H, Tsai C F and MacManus-Driscoll J L 2010 Enhanced flux pinning in  $\text{YBa}_2\text{Cu}_3\text{O}_{7-\delta}$  thin films using Nb-based double perovskite additions *Supercond. Sci. Technol.* **23** 022003
- [2] Macmanus-Driscoll J L, Foltyn S R, Jia Q X, Wang H, Serquis A, Civale L, Maiorov B, Hawley M E, Maley M P and Peterson D E 2004 Strongly enhanced current densities in superconducting coated conductors of  $\text{YBa}_2\text{Cu}_3\text{O}_{7-x} + \text{BaZrO}_3$  *Nat. Mater.* **3** 439–43
- [3] Haugan T, Barnes P N, Wheeler R, Meisenkothen F and Sumption M 2004 Addition of nanoparticle dispersions to enhance flux pinning of the  $\text{YBa}_2\text{Cu}_3\text{O}_{7-x}$  superconductor *Nature* **430** 867–70
- [4] Kang S *et al* 2006 High-performance high- $T_c$  superconducting wires *Science* **311** 1911–4
- [5] Maiorov B, Baily S A, Zhou H, Ugurlu O, Kennison J A, Dowden P C, Holesinger T G, Foltyn S R and Civale L 2009 Synergetic combination of different types of defect to optimize pinning landscape using  $\text{BaZrO}_3$ -doped  $\text{YBa}_2\text{Cu}_3\text{O}_7$  *Nat. Mater.* **8** 398–404
- [6] Wee S H, Gao Y F, Zuev Y L, More K L, Meng J Y, Zhong J X, Stocks G M and Goyal A 2013 Self-assembly of nanostructured, complex, multication films via spontaneous phase separation and strain-driven ordering *Adv. Funct. Mater.* **23** 1912–8
- [7] Xu A, Braccini V, Jaroszynski J, Xin Y and Larbalestier D C 2012 Role of weak uncorrelated pinning introduced by  $\text{BaZrO}_3$  nanorods at low-temperature in  $(\text{Y,Gd})\text{Ba}_2\text{Cu}_3\text{O}_x$  thin films *Phys. Rev. B* **86** 115416
- [8] Toulmonde M, Bouffard S and Studer F 1994 Swift heavy-ions in insulating and conducting oxides-tracks and physical-properties *Nucl. Instrum. Methods Phys. Res. B* **91** 108–23



- [9] Wheeler R, Kirk M A, Marwick A D, Civalé L and Holtzberg F H 1993 Columnar defects in  $\text{YBa}_2\text{Cu}_3\text{O}_{7-\delta}$  induced by irradiation with high-energy heavy-ions *Appl. Phys. Lett.* **63** 1573–5
- [10] Zhu Y, Cai Z X, Budhani R C, Suenaga M and Welch D O 1993 Structures and effects of radiation-damage in cuprate superconductors irradiated with several-hundred-MeV heavy-ions *Phys. Rev. B* **48** 6436–50
- [11] Hardy V, Hervieu M, Provost J, Simon C and Lejay P 2000 Vortex pinning by a gaussian splay of columnar defects in  $\text{YBa}_2\text{Cu}_3\text{O}_7$  *Phys. Rev. B* **62** 691–5
- [12] Civalé L, Marwick A D, Worthington T K, Kirk M A, Thompson J R, Krusinbaum L, Sun Y, Clem J R and Holtzberg F 1991 Vortex confinement by columnar defects in  $\text{YBa}_2\text{Cu}_3\text{O}_7$  crystals: enhanced pinning at high fields and temperatures *Phys. Rev. Lett.* **67** 648–51
- [13] Civalé L 1997 Vortex pinning and creep in high-temperature superconductors with columnar defects *Supercond. Sci. Technol.* **10** A11–28
- [14] Krusinbaum L, Civalé L, Thompson J R and Feild C 1996 Accommodation of vortices to columnar defects: evidence for large entropic reduction of vortex localization *Phys. Rev. B* **53** 11744–50
- [15] Krusinbaum L, Marwick A D, Wheeler R, Feild C, Vinokur V M, Leaf G K and Palumbo M 1996 Pinning with controlled splay configurations of columnar defects; rapid vortex motion at large angles *Phys. Rev. Lett.* **76** 2563–6
- [16] Kwok W K, Paulius L M, Vinokur V M, Petrean A M, Ronningen R M and Crabtree G W 1998 Anisotropically splayed and columnar defects in untwinned  $\text{YBa}_2\text{Cu}_3\text{O}_{7-\delta}$  *Phys. Rev. B* **58** 14594–608
- [17] Sadovskyy I A *et al* 2016 Toward superconducting critical current by design *Adv. Mater.* **28** 4593–600
- [18] Yan Y and Kirk M A 1998 Observation and mechanism of local oxygen reordering induced by high-energy heavy-ion ( $\text{U}^+$ ,  $\text{Au}^+$ ,  $\text{Xe}^+$ ) irradiation in the high- $T_c$  superconductor  $\text{YBa}_2\text{Cu}_3\text{O}_{7-\delta}$  *Phys. Rev. B* **57** 6152–64
- [19] Selvamanickam V *et al* 2009 High performance 2G wires: from R&D to pilot-scale manufacturing *IEEE Trans. Appl. Supercond.* **19** 3225–30
- [20] Xuming X, Lenseth K P, Reeves J L, Rar A, Yunfei Q, Schmidt R M, Yimin C, Yijie L, Yi-Yuan X and Selvamanickam V 2007 High throughput processing of long-length IBAD MgO and epi-buffer templates at SuperPower *IEEE Trans. Appl. Supercond.* **17** 3375–8
- [21] Wen J *et al* 2010 The formation and utility of sub-angstrom to nanometer-sized electron probes in the aberration-corrected transmission electron microscope at the University of Illinois *Microsc. Microanal.* **16** 183–93
- [22] Gauquelin N, Hawthorn D G, Sawatzky G A, Liang R X, Bonn D A, Hardy W N and Botton G A 2014 Atomic scale real-space mapping of holes in  $\text{YBa}_2\text{Cu}_3\text{O}_{6+\delta}$  *Nat. Commun.* **5** 4275
- [23] Zhang F C and Rice T M 1988 Effective Hamiltonian for the superconducting Cu oxides *Phys. Rev. B* **37** 3759–61
- [24] Catana A, Broom R F, Bednorz J G, Mannhart J and Schlom D G 1992 Identification of epitaxial  $\text{Y}_2\text{O}_3$  inclusions in sputtered  $\text{YBa}_2\text{Cu}_3\text{O}_7$  films-impact on film growth *Appl. Phys. Lett.* **60** 1016–8
- [25] Kim K H, Xing H, Zuo J M, Zhang P and Wang H F 2015 TEM based high resolution and low-dose scanning electron nanodiffraction technique for nanostructure imaging and analysis *Micron* **71** 39–45
- [26] Spence J C H and Zuo J M 1992 *Electron Microdiffraction* (New York: Springer Science+Business Media)
- [27] Zandbergen H W, Gronsky R, Wang K and Thomas G 1988 Structure of  $(\text{CuO})_2$  double-layers in superconducting  $\text{YBa}_2\text{Cu}_3\text{O}_7$  *Nature* **331** 596–9
- [28] Findlay S D, Azuma S, Shibata N, Okunishi E and Ikuhara Y 2011 Direct oxygen imaging within a ceramic interface, with some observations upon the dark contrast at the grain boundary *Ultramicroscopy* **111** 285–9
- [29] Fu L F, Browning N D, Ramadan W, Ogale S B, Kundaliya D C and Venkatesan T 2007 Interface and defect structures in  $\text{YBa}_2\text{Cu}_3\text{O}_{7-\delta}$  and Nb:  $\text{SrTiO}_3$  heterojunction *J. Phys. Appl. Phys.* **40** 187–91
- [30] Llordes A *et al* 2012 Nanoscale strain-induced pair suppression as a vortex-pinning mechanism in high-temperature superconductors *Nat. Mater.* **11** 329–36
- [31] Karpinski J, Kaldis E, Jilek E, Rusiecki S and Bucher B 1988 Bulk synthesis of the 81-K superconductor  $\text{YBa}_2\text{Cu}_4\text{O}_8$  at high oxygen-pressure *Nature* **336** 660–2
- [32] Bordet P, Chaillout C, Chenavas J, Hodeau J L, Marezio M, Karpinski J and Kaldis E 1988 Structure determination of the new high-temperature superconductor  $\text{Y}_2\text{Ba}_4\text{Cu}_7\text{O}_{14+x}$  *Nature* **334** 596–8
- [33] Zhang H, Gauquelin N, Botton G A and Wei J Y T 2013 Attenuation of superconductivity in manganite/cuprate heterostructures by epitaxially-induced CuO intergrowths *Appl. Phys. Lett.* **103** 052606
- [34] Kagawa N, Ishida T, Okuda K, Adachi S and Tajima S 2001 Superconducting anisotropy in double-chain  $\text{YBa}_2\text{Cu}_4\text{O}_8$  single crystals *Physica C* **357** 302–4
- [35] Pennycook S J and Jesson D E 1991 High-resolution Z-contrast imaging of crystals *Ultramicroscopy* **37** 14–38
- [36] Cantoni C, Gao Y F, Wee S H, Specht E D, Gazquez J, Meng J Y, Pennycook S J and Goyal A 2011 Strain-driven oxygen deficiency in self-assembled, nanostructured, composite oxide films *ACS Nano* **5** 4783–9
- [37] Grioni M, Vanacker J F, Czyzyk M T and Fuggle J C 1992 Unoccupied electronic-structure and core-hole effects in the x-ray-absorption spectra of  $\text{Cu}_2\text{O}$  *Phys. Rev. B* **45** 3309–18
- [38] Cai Z X and Zhu Y 1998 *Microstructures and Structural Defects in High-Temperature Superconductors* (Singapore: World Scientific) pp 419–75